Met O (APR) Turbulence and Diffusion Note No. 212

A comparison of the Meteorological Office's road surface temperature model with Cardington measurements

by

B.M. Claxton
MRU Cardington

4 January 1995

Met O (APR)
(Atmospheric Processes Research)
Meteorological Office
London Road
Bracknell
Berks, RG12 2SZ

Note

This paper has not been published. Permission to quote from it should be obtained from the Assistant Director, Atmospheric Processes Research Division, Met O (APR), Meteorological Office, London Road, Bracknell, Berkshire, RG12 2SZ.

Met O (APR) Turbulence and Diffusion Note No. 212

A comparison of the Meteorological Office's road surface temperature model with Cardington measurements

by

B.M. Claxton
MRU Cardington

4 January 1995

Met O (APR)
(Atmospheric Processes Research)
Meteorological Office
London Road
Bracknell
Berks, RG12 2SZ

Note

A comparison of the Meteorological Office's road surface temperature model with Cardington measurements

B.M. Claxton
MRU Cardington

Abstract

The Meteorological Office's road surface temperature model was run retrospectively and the predicted road surface temperatures and energy fluxes were compared to Cardington measurements. Over a period of thirty days, using observations as model input, the model was found to have a cool temperature bias of 0.5 ^{o}C, consistent with previous verification studies. It was found that the turbulence scheme the model uses performs better the stronger the wind. Days of light wind caused greater prediction errors than very windy days. Rain was also found to exacerbate errors in the RST model's predictions.

1 Introduction

The Meteorological Office has a service called Open Road which uses a model to predict road surface temperature and moisture. This service is used by highway authorities to aid winter icing policy. The inputs to the road surface temperature [RST] model are forecast air temperature, dew point temperature, wind speed, rain and cloud cover. For details of the model see Rayer 1987 and Thompson 1988.

This investigation compares the the model's predictions of surface temperatures and driving fluxes (sensible, radiant and latent) with measurements made on a section of the A600 that passes by MRU Cardington. The road runs North/South with the site's immediate surroundings being flat fields. A surface site was set up to provide the retrospective input for the RST model. Cloud observations were taken from the observing station at Bedford Airfield. Thermometers were set at various depths in the road so as to obtain temperature profiles which were used to measure the ground flux at the road surface. This experimental ground flux was compared to the ground flux calculated by the RST model. Comparisons were also made between the radiative fluxes calculated by the model and those measured by a radiometer. A measurement of the combined sensible and latent heat flux was obtained as the difference between the measured ground flux and radiative flux.

Data were logged during January, February and March during which time there was sufficient variety in the weather to enable the performance of the RST model to be compared

between broad weather types viz. wet *vs.* dry, strong *vs.* low wind and cloudy *vs.* clear sky.

2 Instrumentation

The instrumentation for this project consists of

- sensors embedded in the A600
- a surface site.

i) Five platinum resistance thermometers (PRTs) were present in the road from a previous study. These five PRTs were embedded in shallow parallel grooves cut into the road. The PRTs were placed in the grooves and covered over with tar of a depth of a few millimetres.

During November 1993, eight more PRTs were set into the road specifically for this study. Unlike the five previous PRTs which were all placed close to the road surface, these additional PRTs were set at various depths, viz; one very close to the surface and one each at $1cm$, $2cm$, $4cm$, $6cm$, $10cm$, $14.7cm$ and $16cm$. The method of embedding these eight PRTs was similar to that used for the previous five in that eight parallel grooves (of various depths) were cut into the road into which the PRTs were placed before being covered over with tar. These eight PRTs were intended to give a temperature profile of the road. However, it should be noted that the material immediately above the PRT at depth x cm was not the normal material of the road but rather x cm of tar. This would introduce some distortion to the temperature profile measured. However, as the grooves were very narrow compared with their depths, and the tar probably had a similar thermal conductivity to the road (which was constructed of a mixture of bitumen and gravel), it was reasonable to assume that the PRTs were to a good approximation in thermal equilibrium with the portions of the road adjacent to them. The measurements made by the PRTs were intended to be accurate to within $0.1\,^{\circ}C$, however during the course of the experiment it became apparent that the calibrations of some of the PRTs tended to drift. This was inferred from plots of temperature profiles in the road. The remaining PRTs seemed to give readings that were consistent amongst themselves throughout the experiment.

Also embedded just beneath the surface of the road and covered with a thin layer of tar were two flux plates. It was intended that these two devices would measure the heat flux at the road surface directly, yet there was a large discrepancy between the measurements of the ground flux made by the flux plates and the ground fluxes calculated from both the measured temperature profiles and the RST model. The flux plates usually gave a measurement that was much less than the magnitude of the expected ground flux. There are several possible explanations for this: firstly, the flux plates are designed to make measurements in soil, secondly there may have been air trapped against the flux plates during installation, thirdly the

flux plates were covered with tar. The first problem arises because the thermal conductivity of soil, which varies much according to composition, is less than that of the material of the road. Hence there is an impedence matching problem. The second possibility, trapped air, would have an insulating effect thus causing the flux plates to give readings of smaller than expected magnitude. Whether there is air trapped between the tar and the plates is unknown, but the plates were installed with due care as regards this potential problem. The third possible source of error, that of the material covering the flux plates being different from the normal material of the road, is significant not only because the tar might insulate the flux plates as trapped air might, but also because the tar forming the surface of the road above the flux plates has different albedo to the normal road surface. Hence there is a difference in the absorption and emissivity coefficients of radiation between the normal road surface and the surface of the tar covering the flux plates. Due to the unsoundness of the direct measurements of ground flux by the flux plates, these measurements were not used to assess the performance of the RST model, using instead ground fluxes calculated from the temperature profiles.

ii) The surface site, located in a grassy field about 100 metres from the road, consisted of a barometer, aspirated humicap, Michell hygrometer, sonic anemometer, radiometer, rain indicator, PRT to measure grass temperature and a pair of dry thermometers (one at height $8.5m$ the other at $1.25m$) to measure screen temperature and the temperature gradient of the air.

The two dry thermometers used to measure the temperature gradient of the air were effectively a thermocouple giving the temperature difference between the junction at $8.5m$ and that at $1.25m$ to $\pm 0.005\,°C$. Hence the error in the measured temperature gradient was less than $\pm 0.001\,K\,m^{-1}$.

The sonic anemometer was positioned on a mast at a height of $10.9m$, the direction the anemometer faced being altered manually according to expectation of wind direction. The wind speed (ms^{-1}) and direction relative to magnetic north as measured by the sonic anemometer were both recorded. The wind speed was measured to an accuracy of $\pm 0.1\,ms^{-1}$ and the accuracy of the wind direction being limited both by the manual sighting of the direction the device was facing and the angle between the sonic direction and the wind direction. For a large range of wind direction relative to the sonic ($\pm 60°$) the predominant error was the sighting of the sonic direction which is estimated to be $\pm 2°$.

The radiometer had both an upward facing plate and a downward facing plate, each protected from precipitation and wind by a plastic dome. Measurements of both the net radiation and the solar radiation were recorded in watts per square metre, with an error of $\pm 5\,Wm^{-2}$. The dome was aspirated so as to reduce measurement errors due to thermal convection.

The rain indicator was a device comprising of a plate with a network of copper rails that was exposed to the sky. Precipitation incident on the copper rails would alter the resistance of the network. The device gave a signal of three volts when the rails were dry and one volt when the rails were covered with a film of water. There was a small heater to dry the plate between precipitous episodes.

Each weekday morning during the period of data collection, the instruments were examined for anything that would impede their normal operation. Hence, it was checked that the motors that aspirated the humicap and the radiometer were working. Overnight dew and rain that had collected on the radiometer dome and the casing of the humicap was removed. The direction the sonic anemometer was facing was compared to the wind direction and altered if the anemometer was facing a direction more than 60^o from the expected wind over the next 24 hours. The measurements made by the barometer, screen height dry thermometer, humicap and sonic anemometer were compared to measurements made by other instruments routinely used at MRU Cardington.

3 Data logging

The measurements made by the the instruments described were logged automatically and continuously using a sampling period of a couple of seconds. The data were averaged in real time and stored in formatted files. Two averaging periods were used, ten minutes and thirty minutes; a dataset for each averaging period was created for each day that data were collected. At around midnight two new datasets would be created to file the data for the forthcoming day. The form of the datasets is given in appendix A.

The times TIM and NHR in the datasets are the times at the centre of the averaging periods. Prior to running the RST model using the meteorological measurements as prognostic input, the datasets were combined so that the ten minute dataset for a particular day contained the data from noon of that day through to noon of the next day.

Figure 1 is a time series plot of the measured road surface temperature. This plot shows that the typical diurnal temperature variation of the road surface was only $5\,^oC$ during January compared with $15\,^oC$ during March. Hence, much greater fluxes are to be found in the road during March. Table 1 gives a brief summary of the data collected for the thirty days for which cloud observations were available. The weather data in this table are for the twenty four hour period beginning at noon of the date for each record. The maximum wind speeds are not for gusts but are the maximum mean wind speeds over ten minute periods. As can be seen from the table there were episodes when the wind was strong over a period of several days, however during February the winds were usually light and the screen temperatures low.

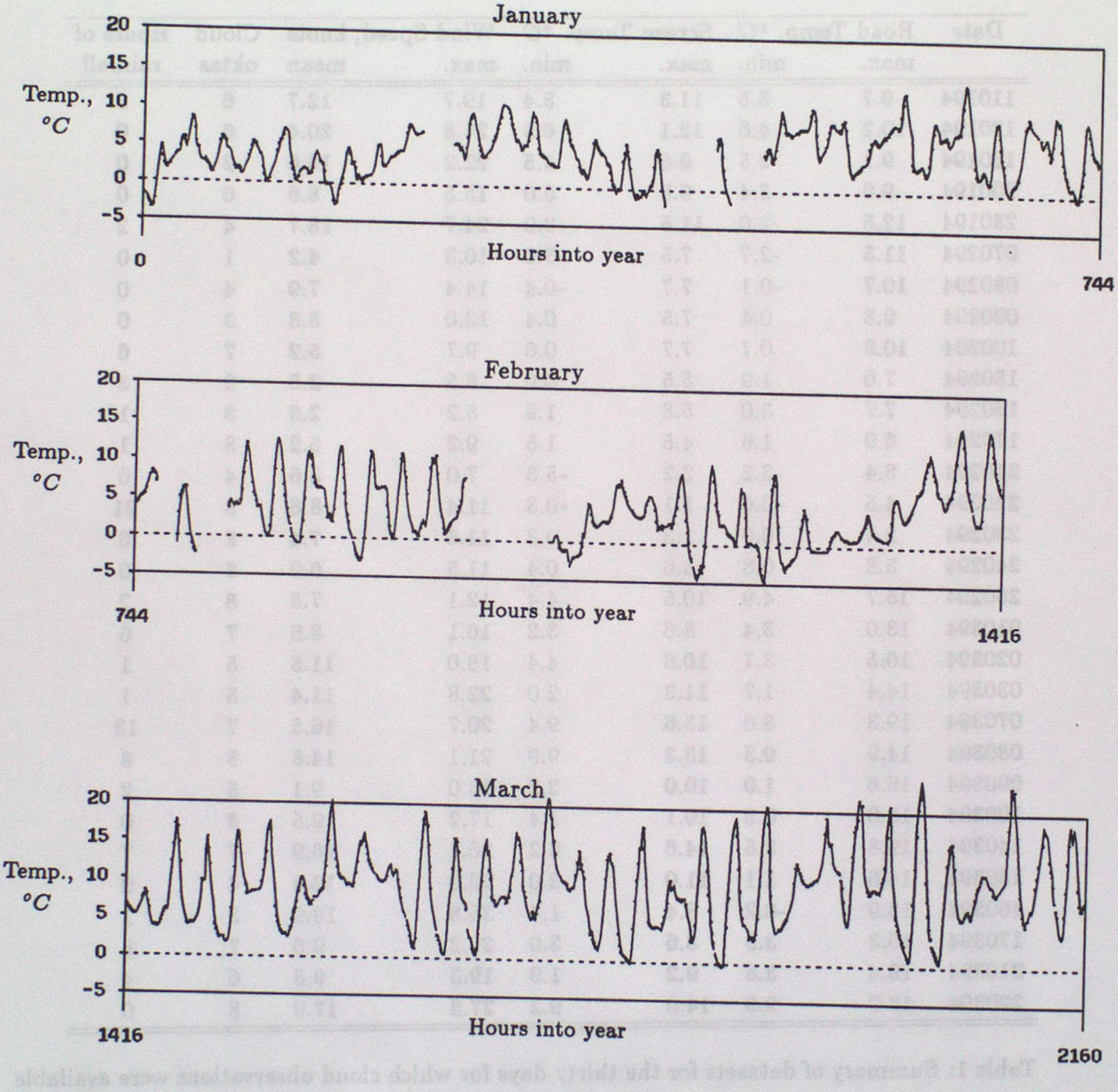

Figure 1: time series of road surface temperature

Date	Road Temp. °C		Screen Temp. °C		Wind Speed, knots		Cloud	Hours of
	max.	min.	max.	min.	max.	mean	oktas	rainfall
110194	9.7	3.5	11.3	5.4	19.7	12.7	6	2
120194	10.2	4.6	12.1	6.9	24.8	20.4	6	0
130194	9.1	2.5	9.6	4.5	22.2	18.6	2	0
200194	9.6	3.4	8.9	5.0	15.5	8.6	6	0
250194	12.5	2.0	11.5	2.0	24.7	18.7	4	2
070294	11.5	-2.7	7.5	-3.0	10.3	4.2	1	0
080294	10.7	-0.1	7.7	-0.4	14.4	7.9	4	0
090294	9.8	0.4	7.5	0.4	13.0	8.3	3	0
100294	10.8	0.7	7.7	0.6	9.7	5.2	7	6
150294	7.0	1.9	5.5	0.6	6.5	2.8	8	3
160294	7.7	3.0	5.8	1.9	5.2	2.6	8	1
170294	6.9	1.6	4.5	1.5	9.2	5.2	8	1
210294	8.4	-3.2	2.2	-5.3	7.0	3.6	4	0
220294	4.5	-0.6	1.1	-0.3	11.4	8.8	8	21
230294	2.4	0.6	1.3	0.3	11.5	7.4	8	6
240294	5.8	0.8	3.6	0.4	11.5	6.0	8	0
280294	15.7	4.9	10.5	4.4	12.1	7.8	8	2
010394	13.0	3.4	8.6	3.2	16.1	8.6	7	6
020394	16.5	3.7	10.6	4.4	18.0	11.5	5	1
030394	14.4	1.7	11.3	2.0	22.8	11.4	5	1
070394	19.3	8.6	13.6	9.4	20.7	16.5	7	13
080394	14.9	9.3	13.3	9.9	21.1	14.8	8	8
090394	16.6	1.0	10.0	2.2	13.0	9.1	5	2
100394	18.0	0.3	10.1	1.4	17.2	9.5	3	0
140394	19.8	8.5	14.6	8.2	26.4	16.9	7	7
150394	14.6	1.1	11.0	2.0	23.0	12.4	4	0
160394	13.9	-0.2	8.4	1.4	25.8	18.9	3	1
170394	16.3	3.8	8.6	3.0	20.2	9.6	7	8
210394	19.4	3.8	9.2	1.9	19.3	9.3	6	4
220394	18.2	9.3	14.0	9.2	27.3	17.9	8	0

Table 1: Summary of datasets for the thirty days for which cloud observations were available

4 Cloud observations

The RST model requires predicted cloud cover as an input. Observations made by the observing station at Bedford Airfield were used. The cloud observations were made hourly, on the hour, during weekdays with a break from 18:00 to 22:00 inclusive. The cloud cover for each hour was classified according to whether the cloud was high, middle or low with the distinctions being made at $600m$ and $240m$. A dataset of cloud observations was created for each day for which the observations made possible, starting at noon and ending at noon the next day, with the period from 18:00 to 22:00 being interpolated from the observations at 17:00 and 23:00.

The cloud data were used by the RST model in predicting the solar radiation incident on the road. A problem with the observations used in this study is that for the frequent occasions when the sky was totally obscured by low cloud, no data are available for high and middle cloud. Thus the cloud observations are not truly prognostic on these days. Another concern about the quality of the cloud data is that five hours a day are devoid of observations. This period covers the evening, which is when the road surface begins to cool. However, it is hoped that the interpolations are reasonable guesses as to the cloud cover during the evenings.

5 Running the model

The ten minute datasets, along with the cloud observations, were used to provide the input for the RST model after being jointly processed to produce a file of input data. The input data for a particular day would contain the hourly data for the RST model inputs, from noon of the day through to noon of the following day. These inputs were:

i. screen temperature

ii. dew point temperature

iii. wind speed

iv. rain prediction

v. oktas of high, middle, low and total cloud cover

In addition the input file also contains hourly values of:

i. measured road surface temperature

ii. road surface heat flux calculated from the road temperature profile

iii. measured solar radiation

iv. measured net radiation

These last four sets of data were used to assess the RST model's forecast of the road surface's temperature and heat flux.

The RST model, at the end of a run, creates a file containing the estimated temperature profile of the road to be used as an initial temperature profile for the next day's run. In order to create a data set of initial temperature profiles, the model was run using the measured radiation data rather than the cloud observations, as radiation data were available for days when no cloud observations were taken. These temperature profiles were used to set up the initial temperature profiles of the road at the start of subsequent runs of the model.

6 Obtaining temperature profiles of the road

Using the PRTs embedded in the road, hourly temperature profiles of the top $16cm$ of the road were obtained by an empirical curve fit. The form of the curve used was;

$$T(z) = a_0 + \sum_{n=1}^{2} e^{-n\alpha z}\{a_n \sin(n\pi\alpha z) + b_n \cos(n\pi\alpha z)\} \tag{1}$$

where α was a constant fixed at $6.25m^{-1}$. The a_n and b_n were found using a least squares technique to fit the curve to the values measured by the PRTs in the road, see appendix C for details. The road surface is most likely to cool to below $0°C$ when the sky is not obscured by clouds. The form of $T(z)$ was chosen so as to provide a curve that would best describe the temperature profile of the road when the insolation flux was sinusoidal, which is most nearly the case during the day with clear sky. The heat equation;

$$\frac{\partial T}{\partial t} = D_T \frac{\partial^2 T}{\partial z^2} \tag{2}$$

where D_T (the thermal diffusivity) is defined as the ratio of the thermal conductivity to the volumetric heat capacity, has an analytic solution for a sinusoidal temperature wave at the surface;

$$T(z,t) = T_s + a_0 \exp\left[-\left(\frac{\omega}{2D_T}\right)^{\frac{1}{2}} z\right] \sin\left[\omega t - \left(\frac{\omega}{2D_T}\right)^{\frac{1}{2}} z + b\right] \tag{3}$$

where T_s is a constant average surface temperature, a_0 the amplitude of the sine wave at $z = 0$, $\omega = (2\pi/p)$ the radial frequency, p the period and b a phase constant. Using values of $1.6Wm^{-1}K^{-1}$ for the thermal conductivity, $1.8MJm^{-3}K^{-1}$ for the heat capacity and estimating the average period of the heating cycle during January, February and March as 17 hours, we find $(\omega/2D_T)^{\frac{1}{2}} \approx 7m^{-1}$. The value of α used in (1) is $6.25m^{-1}$ (that is $1/0.16m$, the inverse depth of the deepest PRT in the road) rather than $7m^{-1}$ in order to make $T(z)$ easier to integrate when calculating the road surface flux. A justification of the values of ω and D_T used is provided by an analysis of the temperature profile of the road during 21^{st} February, which is appendix B.

Although there were eight PRTs fixed in the road, not all were used to obtain the temperature profiles. The PRT at depth $4cm$ was not used at all due to its continuous poor performance. The reliability of some of the other PRTs varied throughout the course of the investigation. The performance of the PRTs was assessed by eye from hourly plots of $T(z)$ against depth z with the corresponding readings from the PRTs marked on the plots. Obvious calibration drifts were then perceptible as PRT readings that were significantly different to those expected if the curve $T(z)$ were to be constructed ignoring the rogue PRTs. A minimum of five PRT readings are required to fix the five a_n and b_n.

7 Calculation of road ground flux from the road temperature profiles

An energy balance scheme, as illustrated by figure 2, was used to calculate the road ground flux using the temperature profiles obtained from the embedded PRTs. The surface heat flux Q_s can be calculated from knowledge of the heat flux Q_d at a depth d, and the rate at which the heat content of the intervening road is changing;

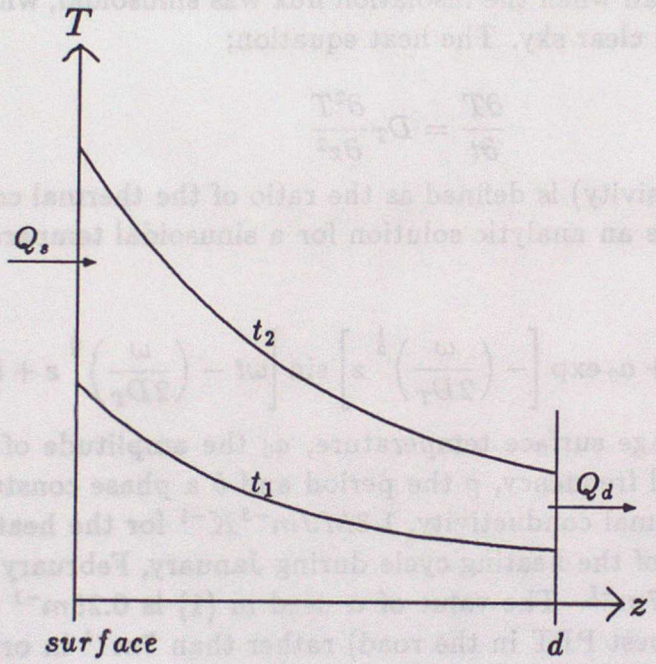

Figure 2: Energy balance scheme

$$Q_s - Q_d = \int_0^d C(z) \frac{\partial T}{\partial t}\, dz \tag{4}$$

where $T(z)$ is the temperature at depth z, as in equation (1), and $C(z)$ is the volumetric heat capacity at depth z. Now, Q_d is given by;

$$Q_d = -k(z) \left.\frac{\partial T}{\partial z}\right|_{z=d} \tag{5}$$

where $k(z)$ is the thermal conductivity at depth z. If $C(z)$ and $k(z)$ are put as constants, C and k, and a finite difference is taken for $\partial T/\partial t$, equation (4) becomes;

$$Q_s(t) \approx C \int_0^d \left\{ \frac{T(t_2) - T(t_1)}{(t_2 - t_1)} \right\} dz - k \left.\frac{\partial T}{\partial z}\right|_{z=d,t} \tag{6}$$

where $t_1 < t < t_2$.
The heat flux Q_d was calculated using the approximation;

$$k \left.\frac{\partial T}{\partial z}\right|_{z=d,t} \approx k \frac{\Delta T}{\Delta z} \tag{7}$$

evaluated using the PRTs at depths 16 cm and 10 cm. Putting the appropriate integral of (1) (see appendix D for details) into (6) gives the formula used to calculate the surface ground flux from temperature measurements in the road as;

$$\begin{aligned} Q_s(t) \;=\; & k\frac{(T_{10}-T_{16})}{0.06} + \frac{C(a_{0,t_2}-a_{0,t_1})}{\alpha(t_2-t_1)} + \\ & \frac{C}{2\alpha(\pi^2+1)(t_2-t_1)}\left\{2(1+e^{-1})[b_{1,t_2}-b_{1,t_1}+\pi(a_{1,t_2}-a_{1,t_1})]+\right. \\ & \left.(1-e^{-2})[b_{2,t_2}-b_{2,t_1}+\pi(a_{2,t_2}-a_{2,t_1})]\right\} \end{aligned} \tag{8}$$

where the a_{n,t_m} and b_{n,t_m} are the a_n and b_n of (1) evaluated at time t_m and T_{10}, T_{16} are the road temperatures at depths 10 and 16 cm.

This calorimetric scheme was used so as to minimise the effect of the possible drift in calibration of the PRTs. An alternative scheme, using the temperature gradient at the the road surface to calculate Q_s, i.e.

$$Q_s = -k(z) \left.\frac{\partial T}{\partial z}\right|_{z=0} \tag{9}$$

is very sensitive to the calibration of the PRTs. For the calorimetric scheme however the PRTs are used to measure changes in temperature over a short time; the change in heat content of the road was calculated over a time interval $(t_2 - t_1)$ of ten minutes. Hence, provided the calibration drifts are on a timescale much greater than ten minutes, the calorimetric scheme is the more robust with respect to the PRTs performance. The flux at depth 16 cm had to be calculated using the temperature gradient, but the flux at this depth was usually very small in comparison to the flux at the surface.

To estimate the error involved in the calculation of the experimental ground flux consider the errors in, (i) calculating the change in heat content of the topmost 16 cm of road, and (ii) calculating the heat flux at depth 16 cm in the road.

i) Approximating (4) and putting G as the contribution to the ground flux due to the changing heat content of the upper part of the road

$$G \approx dC\frac{\Delta T}{\Delta t} \tag{10}$$

hence, the error in G, say δG is

$$\delta G = \frac{dC}{\Delta t}\,\delta(\Delta T). \tag{11}$$

Estimating the error in measurement of a single PRT for the temperature change over the period of ten minutes as $\pm 0.1\,^{\circ}C$ and using five PRTs to fix the shape of the temperature wave,

$$\delta G \approx \pm \frac{0.16 \times 1.8 \times 10^6}{600} \times \frac{0.05}{\sqrt{5}} \approx \pm 11\, W m^{-2} \qquad (12)$$

This will be a random error with mean zero.

ii) In contrast, the error in the calculation of the flux at 16 cm has a potential for a systematic error due to the drift in calibration of either of the PRTs at depths 10 and 16 cm. For an error of $0.1\,^{\circ}C$ in the measurement of the temperature difference between the PRTs at 10 and 16 cm, the error in Q_d, is $\approx 2.5\, W m^{-2}$. Hence the total error in Q_d is the sum of a random error of $\pm 11\, W m^{-2}$ and a systematic bias of $2.5\, W m^{-2}$ for each $0.1\,^{\circ}C$ drift in the relative calibrations of the two deepest PRTs.

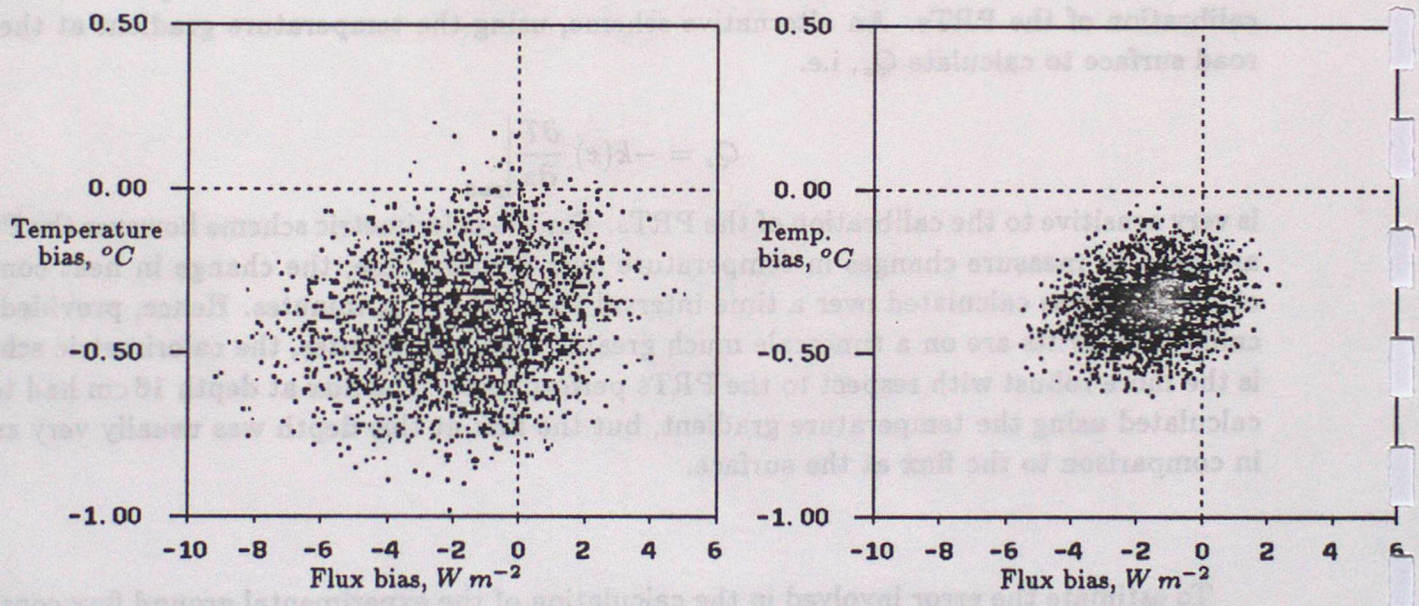

(a) 10 day means (b) 20 day means

Figure 3: scatter plots showing the distribution of temperature and flux biases measured

An indication of the size of any systematic bias can be gauged from figure 3 which shows scatter plots for the temperature and flux biases found between the RST model and the experimental values measured by PRTs for the thirty days of table 1. The temperature bias was calculated as:

$$\text{bias} = \frac{1}{n} \sum_{i=1}^{n} [T_f(i) - T_o(i)] \qquad (13)$$

where $T_f(i)$ is the forecast road surface temperature for a particular hour of the day, $T_o(i)$ being the corresponding observed temperature and n being the number of days to average

over. The flux bias was calculated in a similar way. The experimental values of the ground flux are calculated assuming no systematic bias. In figure 3a each point represents the mean temperature and flux bias of ten randomly chosen days from table 1, three thousand such points are plotted. Figure 3b is as 3a except that each point represents the average of twenty days. The scatter plots show that overall when the RST model calculates a ground flux into the road that is too small, the model predicts road surface temperatures that are too low. This is as expected, although as some of the points in figure 3b are in the sector of positive flux bias and negative temperature bias, this would indicate that perhaps the experimental measure of the ground flux does have a systematic bias of at least $2 W m^{-2}$. This shows up well in figure 3b as the process of averaging over twenty days helps to suppress the random errors. On the basis of the scatter plots and trial plots of figure 4 an offset of $+5.0 W m^{-2}$ was added to the measured ground flux.

A comparison between this study and earlier validation studies of the RST model can be made by using the calculated mean temperature bias over a run of the model. Using the data plotted on figure 4, the mean temperature bias of the RST model, averaged over the thirty days was $-0.5\,^{\circ}C$ and the corresponding flux bias was $-2.5 W m^{-2}$. This is similar to the cool bias reported from the Birmingham trial (Rayer 1987). The scatter plots of figure 3 confirm this.

8 Comparison between the ground fluxes measured and those calculated by the RST model

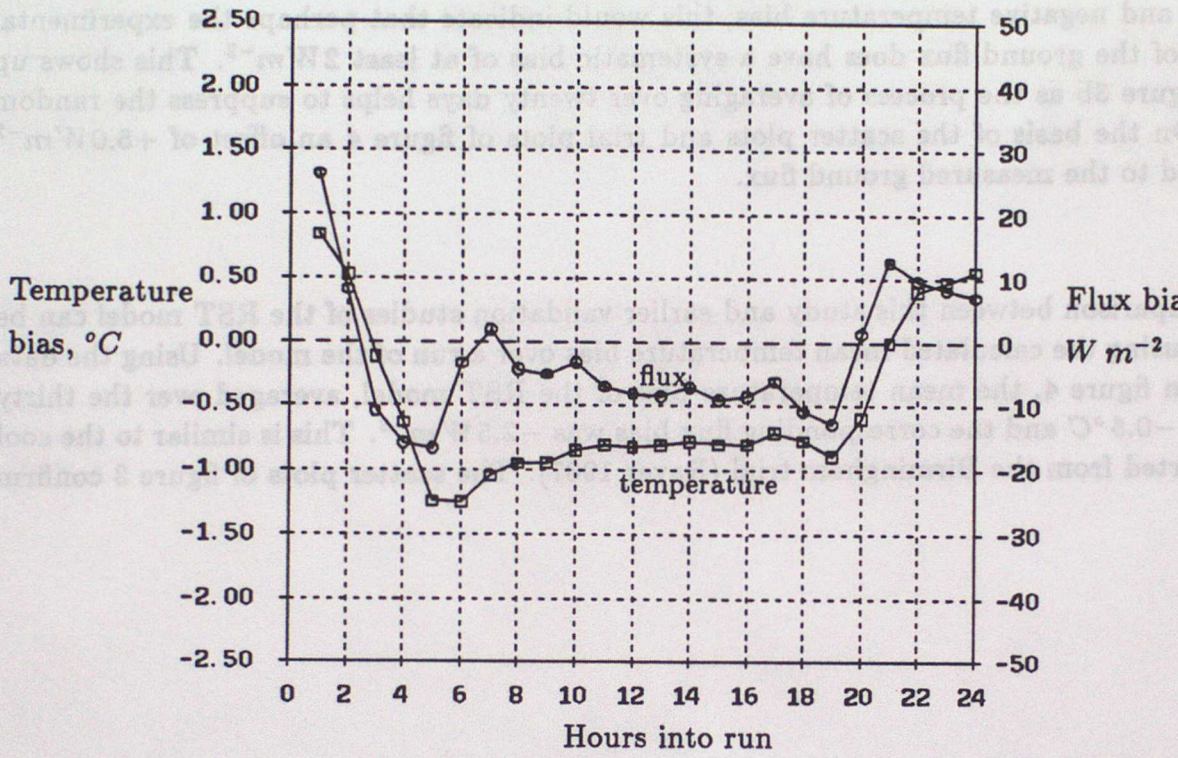

Figure 4: Temperature and flux bias of the RST model averaged over thirty days

The model was run for the thirty days for which there were cloud observations. Both the RST model and the procedure for calculating the ground flux from temperature profiles used values of the thermal conductivity and volumetric heat capacity of $1.6 W m^{-1} K^{-1}$ and $1.8 MJ m^{-3} K^{-1}$ respectively. Figure 4 is a plot showing the temperature bias between the RST model's forecast and the measured road surface temperature superimposed on a plot of the bias between the ground flux as calculated by the RST model and that calculated from the measured temperature profiles. Plotted are the means for the thirty days. A positive temperature bias indicates that the RST model's forecast is too high, a positive flux bias indicates that the RST model's ground flux flowing out of the road is too small. The time coordinate is the time into the model run, all runs starting at noon. Looking at the plot, the temperature bias follows the trend for the ground flux bias, there is a change at around 3pm when the temperature bias changes from being positive just after the flux bias also changes sign. Similarly, in the morning at 9am the temperature bias changes sign after lagging behind the flux bias by just over an hour. It can be seen that during the night the model forecasts road surface temperatures that are lower than those measured by about a degree Celsius. The reverse is the case during daylight hours.

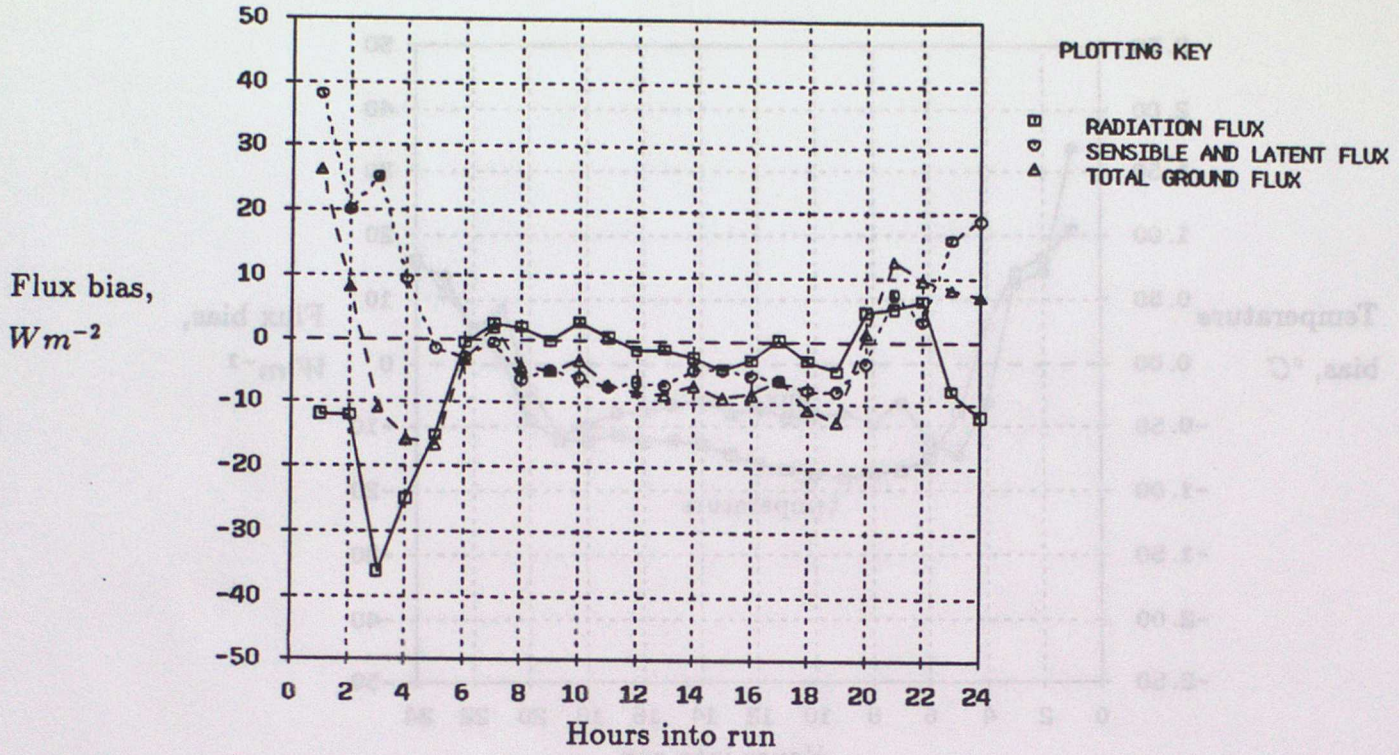

Figure 5: Flux bias averaged over thirty days

This might indicate that the temperature bias is due to the scheme the RST model employs for calculating the radiative flux, which uses cloud cover data. However, figure 5 shows that the sensible and latent heat fluxes at the road surface are in greater error, except at dusk. This plot shows the flux bias of figure 4 decomposed into a bias between the radiative fluxes calculated by the RST model and those measured by the radiometer (after allowing for the fact that the radiometer measured radiative flux over grass rather than road) and a bias on the combined latent and sensible heat flux calculated by the model. An experimental value of the combined latent and sensible heat flux was arrived at by subtracting the measured radiative flux from the measured ground flux. Figure 5 shows that during the daylight hours the net radiation into the road is insufficient but that this is more than compensated for by the combined latent and sensible heat flux out of the road being too small; hence the RST model calculates a total ground flux into the road that is too great during daylight hours. At dusk though the error in the radiative flux reaches a maximum and the under-estimate of the radiative flux into the road leads to the model predicting too rapid a cooling of the road surface. During the night this excessive cooling is reinforced by the turbulent flux into the road being insufficient.

Figure 6 is similar to figure 4 except that figure 6 shows the result of running the model for the same thirty days but using the measured net radiation (after correcting for being measured over grass) in the RST model rather than the radiation scheme involving cloud data. Hence, the flux bias in this case is due to the error in the RST model's latent and sensible

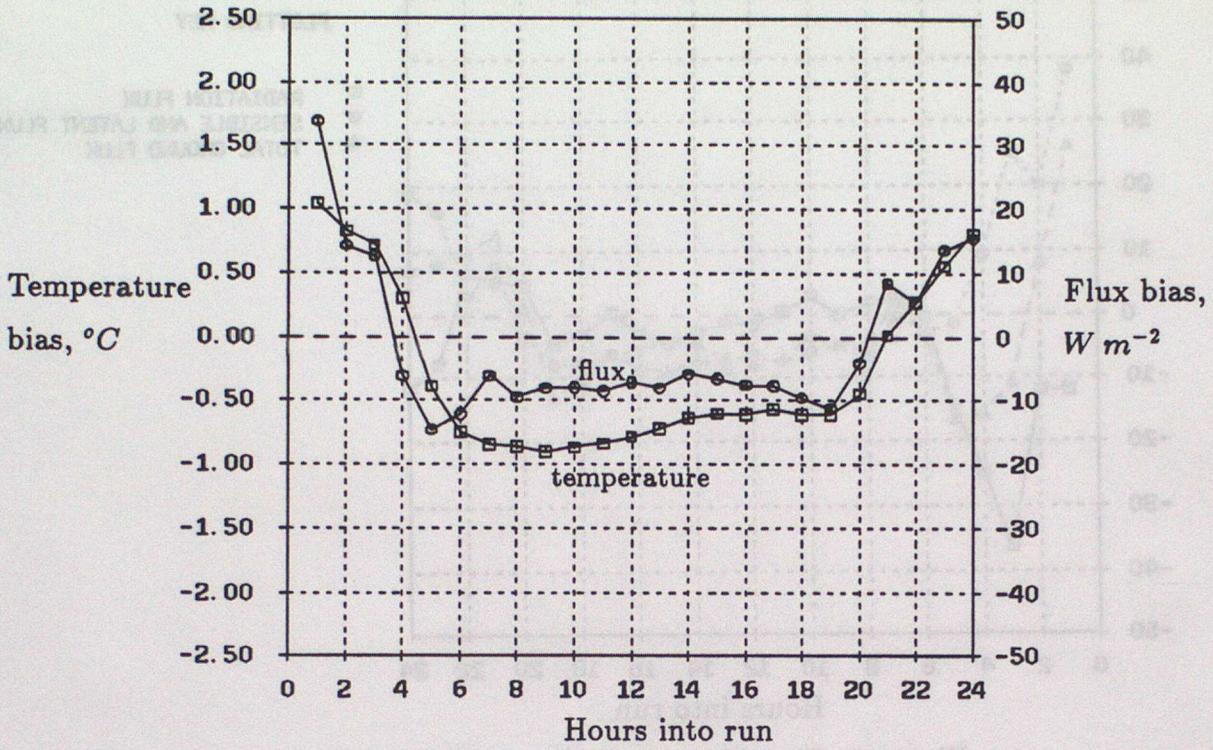

Figure 6: Temperature and flux bias of the RST model averaged over thirty days using measured radiative flux as input to the model

heat flux calculation and the experimental error in the net radiation. This plot clearly shows how temperature bias follows the bias in the combined latent and sensible heat fluxes. The sensible heat flux error is greatest during early afternoon, when the road surface temperatures reach their daily maximum.

The temperature and flux biases were averaged over days during which there was a similarity in a weather variable, so as to assess the RST model's sensitivity to rain, wind and cloud cover. The results of this are plotted in figure 7, which is compiled to the same prescription as figure 4 except that the days averaged over were selected on the basis of a feature of the weather for the duration of the runs. The criteria for selection of days for the plots are:

(a) very cloudy: mean cloud cover greater than 6 oktas
(b) little cloud: mean cloud cover less than 5 oktas
(c) precipitation: precipitation during the RST model run
(d) no precipitation: no precipitation during the RST model run
(e) light winds: mean wind less than 8 knots
(f) high winds: mean wind greater than 10 knots.

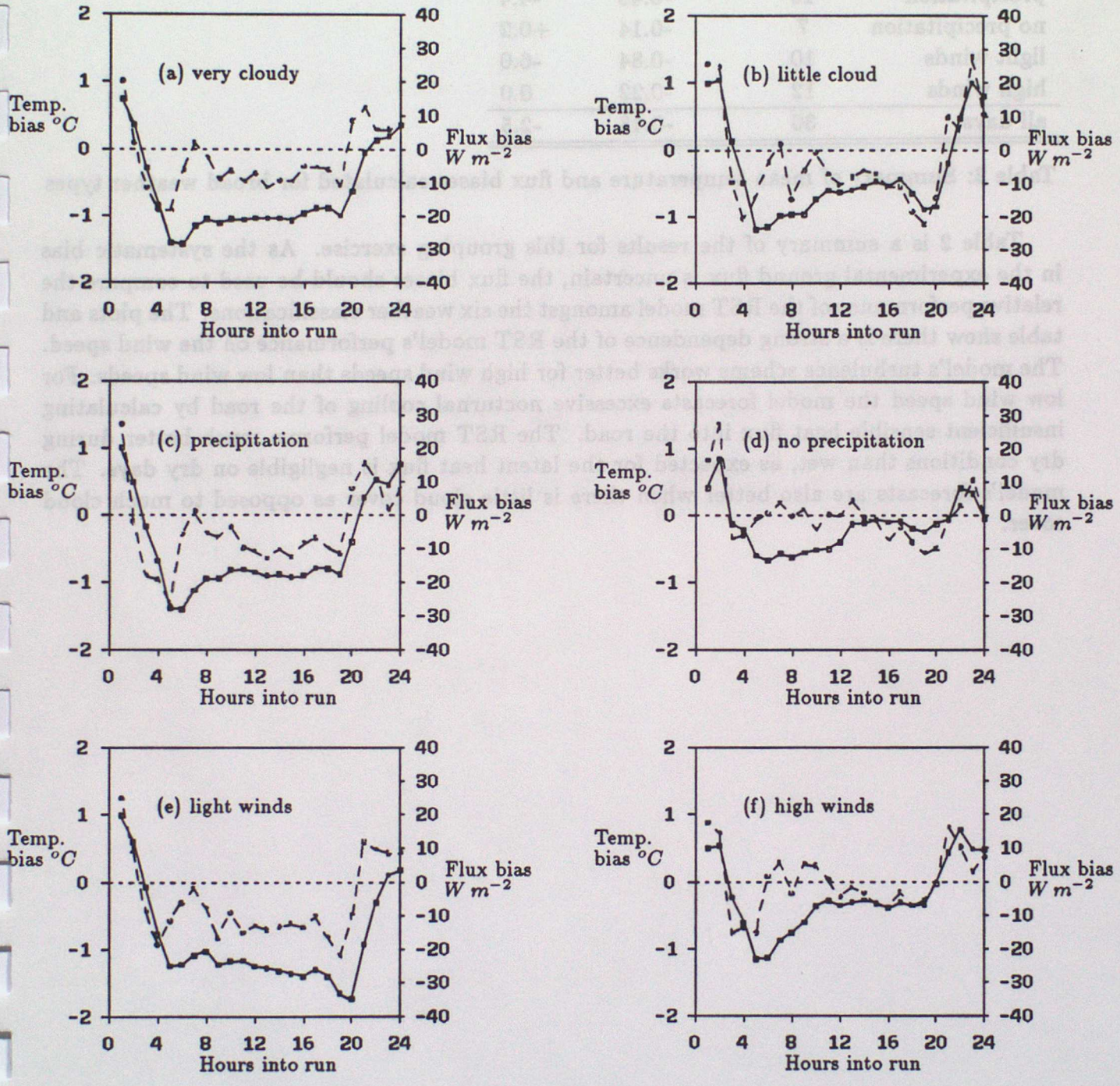

Figure 7: Temperature (full curves) and flux (dotted curves) biases for broad weather types

group	number of days	temp. bias $^{\circ}C$	flux bias $W\,m^{-2}$
very cloudy	14	-0.64	-3.4
little cloud	9	-0.34	-3.2
precipitation	19	-0.48	-4.4
no precipitation	7	-0.14	+0.2
light winds	10	-0.84	-6.0
high winds	12	-0.22	0.0
all days	30	-0.48	-2.5

Table 2: Summary of mean temperature and flux biases calculated for broad weather types

Table 2 is a summary of the results for this grouping exercise. As the systematic bias in the experimental ground flux is uncertain, the flux biases should be used to compare the relative performance of the RST model amongst the six weather classifications. The plots and table show there is a strong dependence of the RST model's performance on the wind speed. The model's turbulence scheme works better for high wind speeds than low wind speeds. For low wind speed the model forecasts excessive nocturnal cooling of the road by calculating insufficient sensible heat flux into the road. The RST model performs much better during dry conditions than wet, as expected for the latent heat flux is negligible on dry days. The model's forecasts are also better when there is little cloud cover as opposed to much cloud cover.

9 Traffic census

A traffic census of the A600 was undertaken for the week 16^{th} to 23^{rd} February inclusive. The results of this survey are shown in figure 8 where figure 8a shows the mean traffic flow on a week day and figure 8b shows the mean traffic flow over the weekend. Rush-hour peaks are features of figure 8a. If the RST model were to incorporate traffic into the scheme for calculating the sensible heat flux at the road surface, then this would increase the sensible heat flux out of the road during the daylight hours, thus reducing the error in the calculated sensible heat flux during daylight hours.

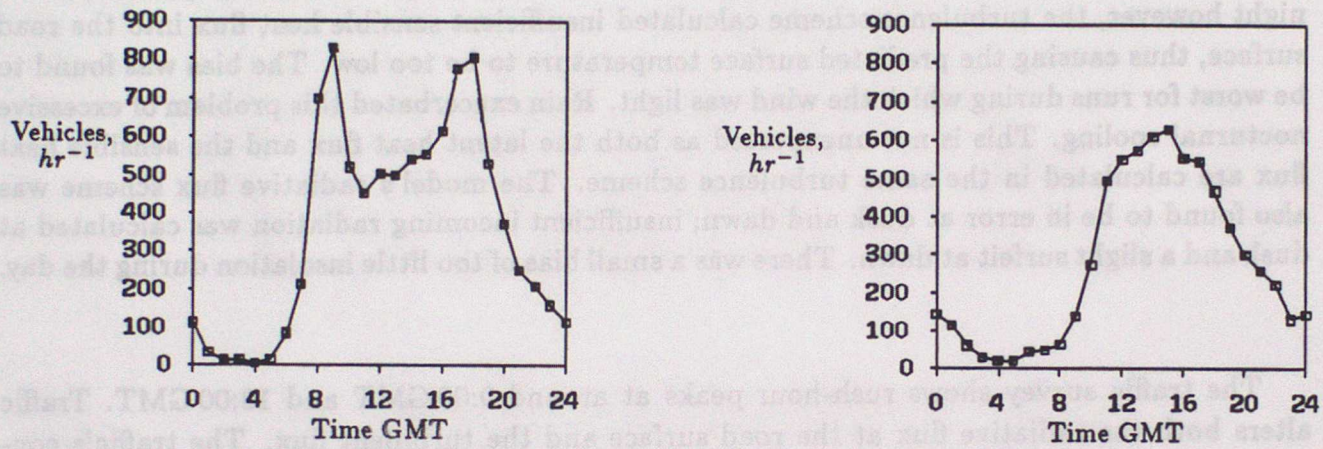

(a) mean weekday traffic flow

(b) mean weekend traffic flow

Figure 8: Traffic census of A600

On days of light winds the turbulence created by vehicles will more significantly contribute to the sensible heat flux than on more windy days. This is an important consideration because the days with the coldest road surface temperatures during the winter tend to be days when there is little wind. As can be seen from figure 7e the RST model calculates insufficient sensible heat flux into the road during calm nights. Also, especially during the winter, motor vehicles are net radiators into the road. These enhanced radiative and sensible heat fluxes into the road would go some way to counteract the problem of excessive nocturnal cooling forecast by the RST model.

10 Conclusion

An overall cool temperature bias of $0.5\,^{\circ}C$ between the RST model's predicted road surface temperature and that measured was found, which is consistent with previous verification studies (Rayer 1987, Thornes and Shao 1991). A cause of the temperature bias was shown to be errors in the flux calculations of the model, these fluxes driving the model's finite difference scheme for solving the heat conduction equation (2). Whilst the radiation scheme that uses predicted cloud cover was found to have a systematic bias of calculating insufficient insolation incident on the road, the greater error appeared to be with the sensible and latent heat fluxes. The turbulence scheme calculated insufficient sensible heat loss at the road surface during the daylight hours, more than compensating for the error in the radiative flux, causing the RST model's predicted road surface temperature to be too high during daylight hours. At night however, the turbulence scheme calculated insufficient sensible heat flux into the road surface, thus causing the predicted surface temperature to be too low. The bias was found to be worst for runs during which the wind was light. Rain exacerbated this problem of excessive nocturnal cooling. This is not unexpected as both the latent heat flux and the sensible heat flux are calculated in the same turbulence scheme. The model's radiative flux scheme was also found to be in error at dusk and dawn; insufficient incoming radiation was calculated at dusk and a slight surfeit at dawn. There was a small bias of too little insolation during the day.

The traffic survey shows rush-hour peaks at around 9:00 GMT and 18:00 GMT. Traffic alters both the radiative flux at the road surface and the turbulent flux. The traffic's contribution to the turbulent flux would help ameliorate the problem with excessive nocturnal cooling and daytime warming. The contribution to the radiative flux would also help counter the nocturnal cool bias.

11 References

Monteith, J.L., 1973: Principles of Environmental Physics. London, Edward Arnold.

Rayer, P.J., 1987: The Meteorological Office forecast road surface temperature model. *Meteorol Mag*, **116**, 180-191.

Thompson, N., 1988: The Meteorological Office road surface temperature prediction model. *In* Proceedings of the 4^{th} International Conference on Weather and Road Safety, Florence, 8-10 November 1988. Standing International Road Weather Commission.

Thornes, J.E. and Shao, J., 1991: A comparison of UK road ice prediction models. *Meteorol Mag*, **120**, 51-57.

APPENDICES

A Datasets

The form of the ten and thirty minute datasets created was:

U DIRN
wind speed (ms^{-1}), wind direction relative to magnetic North

UHB VHB WHB TSHB
U,V,W components of the wind (ms^{-1}), T sonic (Deg S)

PPNB SOLB RADB PRSB
rain (3=0%,1=100%), solar radiation (Wm^{-2}), net radiation (Wm^{-2}), pressure (hPa)

RHLB TGRB WTB
rh humicap % (at $1.2m$),temp. of grass (°C), covariance WT from sonic

MLB MLFB
dew Michell low (°C), flag Michell low

P1B P3B P4B
road surface PRTs (°C)

P5B P6B
road surface PRTs (°C)

P1AB P2AB P3AB P4AB
road PRTs at depths $0cm$,$1cm$,$2cm$,$4cm$ (°C)

P5AB P6AB P7AB P8AB
road PRTs at depths $6cm$,$10cm$,$14.7cm$,$16cm$ (°C)

AHIB ALOB FP1B FP2B
ASL-high ($\approx 8.5m$) (°C),ASL-low ($1.25m$) (°C), flux plate 1 (Wm^{-2}), flux plate 2 (Wm^{-2})

TIM
decimal hours since midnight

NHR
decimal hours since start of year

ZHI DIRNI
sonic height (m), sonic direction relative to magnetic North

B Surface temperature wave of 21st February

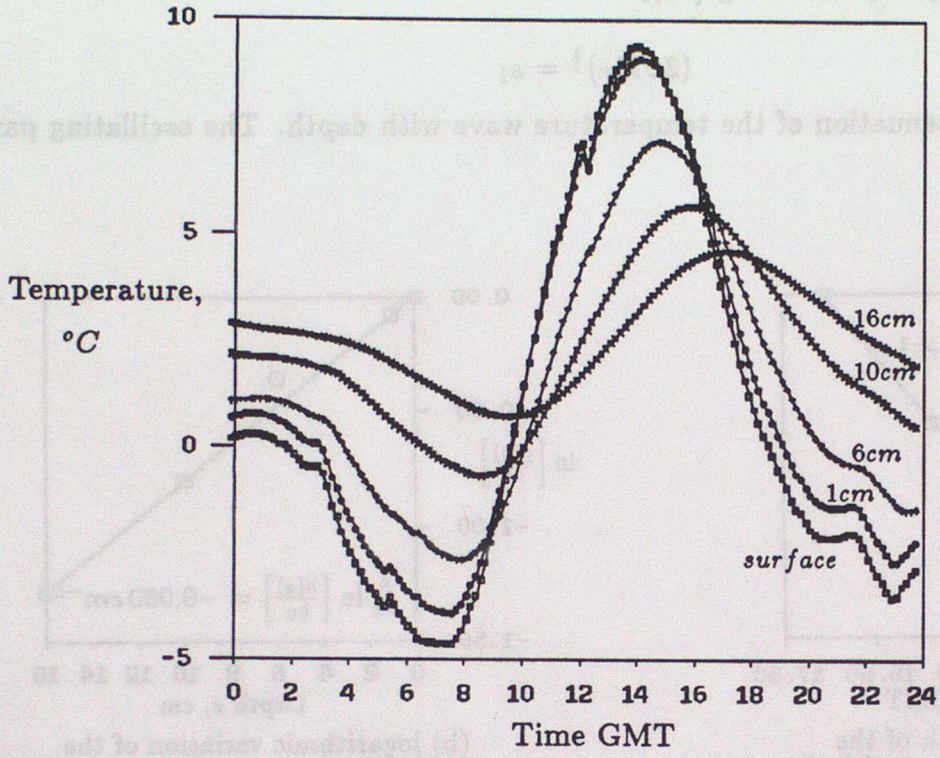

Figure 9: Temperature plot for 21st February

The insolation on 21st February was very nearly sinusoidal, resulting in a near sinusoidal temperature wave at the road surface during the daylight hours. This is shown by figure 9 which shows how the temperatures measured by the PRTs in the road varied sinusoidally during the daylight hours.
Treating the temperature wave at the surface as sinusoidal, ie,

$$T(0,t) = T_s + a_0 \sin(\omega t) \tag{14}$$

where a_0 is the amplitude of the surface temperature wave and ω the angular frequency of oscillation, the solution of the heat conduction equation (2) is (Monteith 1973),

$$T(z,t) = T_s + a_0 \exp\left[-\left(\frac{\omega}{2D_T}\right)^{\frac{1}{2}} z\right] \sin\left[\omega t - \left(\frac{\omega}{2D_T}\right)^{\frac{1}{2}} z + b\right] \tag{15}$$

The position of any fixed point on the temperature wave (for example a maximum or minimum) is specified by a constant phase angle, ie;

$$\omega t - \left(\frac{\omega}{2D_T}\right)^{\frac{1}{2}} z + b = \text{constant} \tag{16}$$

Differentiating (16) with respect to time, and rearranging gives;

$$\frac{\partial z}{\partial t} = (2\omega D_T)^{\frac{1}{2}} \tag{17}$$

which is the speed with which signals of frequency ω travel down through the road. In figure 10a the depth of the maximum of the temperature wave as it passes into the road is plotted against time. The gradient of the best fit line (drawn ignoring the point at 6cm) is $\partial z/\partial t$. Hence, calling this slope s_1 and using (17),

$$(2\omega D_T)^{\frac{1}{2}} = s_1 \tag{18}$$

Now consider the attenuation of the temperature wave with depth. The oscillating part of

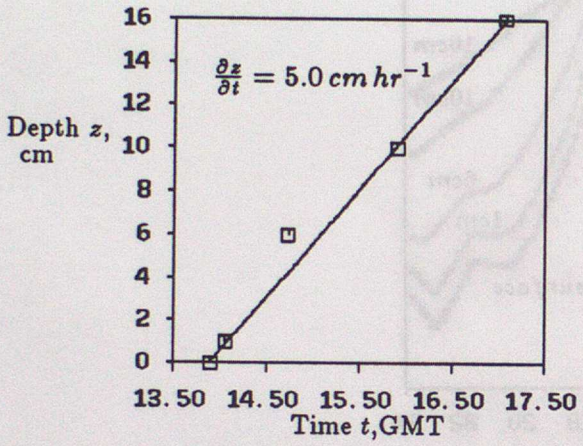

(a) variation in depth of the temperature maximum with time

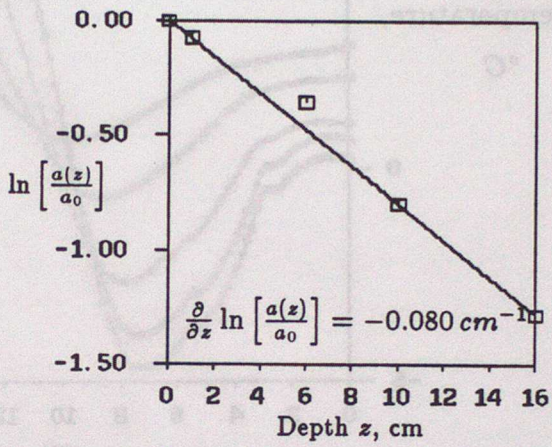

(b) logarithmic variation of the temperature wave amplitude with depth

Figure 10: Evolution of the temperature wave

the temperature wave varies as $a(z)\sin(\omega t - kz)$ where $a(z)$, the amplitude at depth z, decays exponentially as $a_0 \exp[-(\omega/2D_T)^{\frac{1}{2}}z]$. Hence;

$$\frac{a(z)}{a_0} = \exp\left[-\left(\frac{\omega}{2D_T}\right)^{\frac{1}{2}} z\right] \tag{19}$$

Taking logarithms and differentiating with respect to z gives;

$$\frac{\partial}{\partial z}\left[\ln\left(\frac{a(z)}{a_0}\right)\right] = -\left(\frac{\omega}{2D_T}\right)^{\frac{1}{2}} \tag{20}$$

Figure 10b shows $\ln[a(z)/a_0]$ plotted against depth for 21st February. Using (20) and calling the gradient of the best fit line in figure 10b s_2, we have;

$$\left(\frac{\omega}{2D_T}\right)^{\frac{1}{2}} = -s_2 \tag{21}$$

Combining (18) and (21) we have;

$$D_T = -\frac{s_1}{2s_2} \tag{22}$$

and

$$\omega = -s_1 s_2 \tag{23}$$

As indicated on figure 10 the values of s_1 and s_2 for 21^{st} February are $5.0\,cm\,hr^{-1}$ and $-0.080\,cm^{-1}$ respectively. Putting these values in (22) and (23) gives $D_T = 8.7 \times 10^{-7}\,m^2\,s^{-1}$ and a period $(2\pi/\omega)$ of $15.7\,hr$. The value of the parameter α used in (1) for the empirical curve fitting is $6.25\,m^{-1}$ which is close to the value of $-s_2$ $(8.0\,m^{-1})$ to which α corresponds.

C Curve fitting

Suppose a set of p points (X_i, Y_i) with $i = 1, 2, ..., p$ and a curve to fit through the points of the form

$$y = \sum_{j=0}^{n} a_j f_j(x) \tag{24}$$

where the $f_j(x)$ are known. Substitute the X_i into (24) so that

$$y_i = \sum_{j=0}^{n} a_j f_j(X_i)\,.$$

Define the residual ξ_i as the difference between Y_i and y_i,

$$\xi_i = Y_i - y_i\,.$$

Write the sum of the squares of the residuals as S,

$$S = \sum_{i=1}^{p} (\xi_i^2) = \sum_{i=1}^{p} \left\{ Y_i - \sum_{j=0}^{n} a_j f_j(X_i) \right\}^2 \tag{25}$$

Now, S will be zero only if the curve is a perfect fit, otherwise S will be positive. For the optimum set of a_j, S will be a minimum, say S_m. Now suppose the a_j are optimal, and put $a_j + \epsilon_j$ into (25);

$$S_\epsilon = \sum_{i=1}^{p} \left\{ Y_i - \sum_{j=0}^{n} (a_j + \epsilon_j) f_j(X_i) \right\}^2$$

and $S_\epsilon \geq S_m$ for all values of ϵ_j. Now,

$$S_\epsilon = \sum_{i=1}^{p} \left[\left\{ Y_i - \sum_{j=0}^{n} a_j f_j(X_i) \right\} - \sum_{j=0}^{n} \epsilon_j f_j(X_i) \right]^2$$

Hence,

$$S_\epsilon = \sum_{i=1}^{p}\left\{Y_i - \sum_{j=0}^{n} a_j f_j(X_i)\right\}^2 - 2\sum_{i=1}^{p}\left\{Y_i - \sum_{j=0}^{n} a_j f_j(X_i)\right\}\left\{\sum_{j=0}^{n}\epsilon_j f_j(X_i)\right\} + \sum_{i=1}^{p}\left\{\sum_{j=0}^{n}\epsilon_j f_j(X_i)\right\}^2 \tag{26}$$

The first term on the right of (26) is S_m. As $S_\epsilon - S_m \geq 0$,

$$-2\sum_{i=1}^{p}\left\{Y_i - \sum_{j=0}^{n} a_j f_j(X_i)\right\}\left\{\sum_{j=0}^{n}\epsilon_j f_j(X_i)\right\} + \sum_{i=1}^{p}\left\{\sum_{j=0}^{n}\epsilon_j f_j(X_i)\right\}^2 \geq 0\,. \tag{27}$$

This is true for all ϵ_j. If the ϵ_j are very small, the second term in (27) will be small compared to the first term and may be neglected. Then (27) will only be true if the first term vanishes, otherwise the ϵ_j could be chosen so as to make the first term negative. Hence;

$$\sum_{i=1}^{p}\left\{Y_i - \sum_{j=0}^{n} a_j f_j(X_i)\right\}\left\{\sum_{j=0}^{n}\epsilon_j f_j(X_i)\right\} = 0\,.$$

This is true for all ϵ_j, so the coefficients of the ϵ_j's must vanish. This gives $n+1$ equations, enabling the a_j to be found;

$$\sum_{i=1}^{p}\left\{Y_i f_k(X_i) - \sum_{j=0}^{n} a_j f_j(X_i) f_k(X_i)\right\} = 0 \qquad {\scriptstyle k=0,1,2,\ldots,n.} \tag{28}$$

The set of equations (28) can be solved by Gaussian elimination to give the coeffecients a_j for the curve (24).

D Integration of temperature profiles

To integrate a temperature profile curve (1) over depth z let

$$I = \int_0^{\xi} e^{-\alpha n z} \sin(\alpha n \pi z)\, dz \tag{29}$$

and

$$J = \int_0^{\xi} e^{-\alpha n z} \cos(\alpha n \pi z)\, dz \tag{30}$$

Now form $K = J + iI$ where $i = \sqrt{-1}$ and we have,

$$K = J + iI = \int_0^{\xi} e^{(i\pi - 1)n\alpha z}\, dz \tag{31}$$

for which the solution is,

$$K = \frac{(1 + i\pi)}{n\alpha(\pi^2 + 1)} \left\{1 - e^{(i\pi - 1)n\alpha\xi}\right\} \tag{32}$$

Putting in $\xi = 1/\alpha$ and separating the real and imiginary parts of K we have,

$$J = \Re[K] = \frac{[1 + (-1)^{n+1} e^{-n}]}{n\alpha(\pi^2 + 1)} \tag{33}$$

and

$$I = \Im[K] = \pi \frac{[1 + (-1)^{n+1} e^{-n}]}{n\alpha(\pi^2 + 1)} \tag{34}$$

Using (33) and (34) together with (1) we get,

$$\int_0^{\frac{1}{\alpha}} T(z) dz = \frac{a_0}{\alpha} + \frac{(1 + e^{-1})}{\alpha(\pi^2 + 1)}(b_1 + a_1\pi) + \frac{(1 - e^{-2})}{2\alpha(\pi^2 + 1)}(b_2 + a_2\pi) \tag{35}$$